

Improved Neuronal Tract Tracing using Manganese Enhanced Magnetic Resonance Imaging with Fast T_1 Mapping

Kai-Hsiang Chuang and Alan Koretsky*

There has been growing interest in using manganese-enhanced MRI (MEMRI) to detect neuronal activation, neural architecture, and neuronal connections. Usually Mn^{2+} produces a very wide range of T_1 change. In particular, in neuronal tract tracing experiments the site of Mn^{2+} injection can have very short T_1 , while distant regions have small T_1 reductions, primarily due to dilution of Mn^{2+} . Most MEMRI studies use T_1 -weighted sequences, which can only give optimal contrast for a narrow range of T_1 changes. To improve sensitivity to the full extent of Mn^{2+} concentrations and to optimize detection of low concentrations of Mn^{2+} , a fast T_1 mapping sequence based on the Look and Locker technique was implemented. Phantom studies demonstrated less than 6.5% error in T_1 compared to more conventional T_1 measurements. Using center-out segmented EPI, whole-brain 3D T_1 maps with 200- μm isotropic resolution were obtained in 2 h from rat brain. Mn^{2+} transport from the rat olfactory bulb through appropriate brain structures could be detected to the amygdala in individual animals. The method reliably detected less than 7% reductions in T_1 . With this quantitative imaging it should be possible to study more extensive pathways using MEMRI and decrease the dose of Mn^{2+} used. Magn Reson Med 55:604–611, 2006. Published 2006 Wiley-Liss, Inc.†

Key words: manganese enhanced MRI; T_1 map; neuronal tract tracing; molecular imaging; olfactory pathways

The use of divalent manganese ions (Mn^{2+}) as functional, molecular, and anatomic contrast agent for MRI of the brain has drawn increasing attention in recent years (1–7). Mn^{2+} , a Ca^{2+} analog, can enter excitable cells through voltage-gated calcium channels (8) and can be transported by microtubules in axons toward the projecting neurons (9). In addition, Mn^{2+} will differentially accumulate in different areas of the brain (10,11). These interesting biologic properties, combined with the fact that Mn^{2+} is an effective MRI relaxation agent, have enabled manganese-enhanced MRI (MEMRI) to be used to observe neuronal activation following specific stimulations (12–15), to perform anterograde neuronal tract tracing in a number of neural systems (16–23), and to enable MEMRI to visualizing neuroarchitectures not previously detectable by MRI (24,25).

Although large signal changes are usually measured in MEMRI using T_1 -weighted (T_1W) sequences, there is still need to improve the detectability of Mn^{2+} . For example, in many MEMRI neuronal tract-tracing experiments there is a broad range of T_1 changes that need to be detected—from very large T_1 changes at the Mn^{2+} injection site to very small changes in regions distant from the injection site. This is because when Mn^{2+} is transported along axons and across synapses, its concentration is diluted to a level that is difficult to detect. Another reason for optimizing the detection sensitivity of MEMRI is to reduce the doses used so as to avoid neurotoxicity that can be caused by high levels of manganese. For instance, it is well known that chronic exposure to excess manganese will cause neurologic effects similar to Parkinson's disease (26).

The large majority of MEMRI studies have relied on T_1W imaging to detect signal changes caused by the shortening of T_1 . Common ways to obtain T_1W contrast are spin-echo or gradient-echo sequences with short repetition time (TR) and/or large flip angle (FA). Stronger T_1W can be achieved with an inversion preparatory pulse. To improve the detectability of a T_1 contrast agent, imaging parameters, like the TR, FA, and/or inversion time (TI), can be optimized according to the expected concentration of the contrast agent and signal-to-noise ratio (SNR) (27). More sophisticated 3D T_1W methods, such as magnetization-prepared rapid gradient-echo (21), modified driven equilibrium Fourier transform (28,29), or optimized tissue-nulling echo-planar imaging (EPI) (30), can be optimized for specific T_1 values and have been used to delineate gray/white matter contrast in humans at high field (31,32) as well as for MEMRI studies (19). One shortcoming of these approaches is when T_1 changes span a wide range, i.e., from 300 to 2000 ms, as can be the case with MEMRI experiments (33), several sets of the optimized imaging parameters and therefore several images are needed. In addition, when the concentration of the contrast agent is very low, the above methods are not ideal to provide detectable contrast for small T_1 changes. Statistical mapping of the averaged data from different experimental animals has been used in MEMRI neuronal tract tracing to increase the sensitivity of T_1W imaging (34). However, the detectability is still limited by the sensitivity of the T_1W sequence used and it is more difficult to follow changes in individual animals.

Another approach is to produce T_1 maps to visualize and quantitate T_1 contrast. T_1 mapping provide sensitivity to the full range of T_1 and has the potential to quantify the tissue concentrations of the contrast agent with the knowledge of the relaxivity of the agent used. An additional benefit is that it is less affected by the signal inhomogene-

Laboratory of Functional and Molecular Imaging, National Institute of Neurological Disorders and Stroke, NIH, Bethesda, Maryland, USA.

Grant sponsor: Intramural Research Program of the NIH, NINDS.

*Correspondence to: Alan P. Koretsky, Laboratory of Functional and Molecular Imaging, National Institute of Neurological Disorders and Stroke, National Institutes of Health, 10 Center Drive, 10/B1D728, Bethesda, MD 20892-1065, USA. E-mail: KoretskyA@ninds.nih.gov

Received 30 August 2005; revised 4 November 2005; accepted 6 November 2005

DOI 10.1002/mrm.20797

Published online 7 February 2006 in Wiley InterScience (www.interscience.wiley.com).

Published 2006 Wiley-Liss, Inc. † This article is a US Government work and, as such, is in the public domain in the United States of America. 604

ity that may arise in the images, such as due to RF inhomogeneity. A major drawback of T_1 mapping techniques is that they are usually very time consuming. Indeed, the time needed to generate T_1 maps of sufficient resolution is probably why no MEMRI studies have been reported that made routine use of quantitative T_1 measurements. The reason why conventional spin-echo inversion-recovery (IR) or saturation-recovery T_1 mapping methods need long imaging time is that they rely on repeated measurements with different TIs or saturation times. For example, the optimized 2D modified fast IR (MFIR) spin-echo T_1 measurement with the TR of three times the longest T_1 and four different TIs will take at least an hour to acquire a 128×128 matrix (35). Although data acquisition could be accelerated by EPI, conventional T_1 mapping techniques would be too long for in vivo, high-resolution 3D mapping.

Fast T_1 mapping methods have been developed to overcome some of the time limitations. Fast gradient echo sequences that use variable flip angles with steady-state free precession data acquisition can generate T_1 maps (36). Another fast T_1 measurement method is the Look-Locker (LL) technique, which samples multiple time points during signal recovery (37). This method can significantly reduce scanning time without sacrificing accuracy. This method has been shown to have almost the same efficiency as the spin-echo IR method in terms of the SNR per unit time (38). In the present study we have begun to develop approaches that enable T_1 mapping for MEMRI neuronal tract tracing. Whole-brain, 2D multi-slice and 3D EPI LL T_1 mapping methods were implemented and optimized for detecting low concentrations of Mn^{2+} . This fast LL technique was tested by tracing the rat olfactory pathways after stereotaxic Mn^{2+} injection into the olfactory bulb. Results indicate that tracing of Mn^{2+} as far as the amygdala can be readily detected in individual animals using T_1 maps.

MATERIALS AND METHODS

Look-Locker T_1 mapping

In a typical LL T_1 measurement, N RF pulses of the same FA, α , are used to sample multiple time points with a fixed interexcitation interval, τ , during the relaxation from an inversion pulse. The signal evolution has been derived in Ref. (37) and earlier imaging version of this technique (39). In brief, the partially relaxed longitudinal magnetization, $M(n)$, before each excitation pulse can be described by an exponential recovery with time constant T_1^* :

$$M(n) = M(\infty) - [M(\infty) - M(0)]e^{-n\tau/T_1^*}, n = 0, 1, \dots, N-1. \quad [1]$$

In Eq. [1],

$$M(\infty) = M_{eq} \frac{1 - e^{-\tau/T_1}}{1 - e^{-\tau/T_1^*}}, \quad [2]$$

where M_{eq} is the equilibrium longitudinal magnetization and the effective longitudinal relaxation time constant, T_1^* , is related to the actual T_1 , α , and τ by

$$\frac{1}{T_1^*} = \frac{1}{T_1} - \frac{\ln \cos(\alpha)}{\tau}. \quad [3]$$

Ideally, if the exact FA at each pixel is known, the T_1 can be easily calculated from Eq. [3] after obtaining T_1^* from a three-parameter fit to Eq. [1]. However, the B_1 field inhomogeneity from the imperfect excitation pulse and the RF coil profile makes the FA differ from the intended value. To solve the actual T_1 , the relation between $M(\infty)$ and $M(0)$ can be used. For example, when $\tau \ll T_1^*$ and the TR is long enough such that $M(0) \approx -M_{eq}$, Eq. [2] can be simplified by the first-order approximation and T_1 can be approximated by $T_1^*M(0)/M(\infty)$ (40).

Since the error in T_1 measurement is related to the T_1 , τ , and FA, generally longer τ is needed for accurate measurement of longer T_1 (41). When using a long τ to optimize the accuracy for detecting low Mn^{2+} concentrations, the above approximation for deriving T_1 will be inaccurate. Furthermore, it would be incorrect to assume $M(0) = -M_{eq}$, especially in a multislice acquisition. Usually, a very short inversion delay is used to achieve the maximal dynamic range and hence could be neglected in approximating T_1 . However, when using a lot of slices to cover the whole brain, this time delay will be different for each slice and cannot be ignored. Here, we used a more general algorithm to calculate T_1 . Assuming the longitudinal magnetization before each inversion pulse has reached steady state, then $M(0)$ can be expressed as

$$M(0) = M_{eq}(1 - e^{-T_d/T_1}) - M_{ss}e^{-T_d/T_1}, \quad [4]$$

where M_{ss} is the longitudinal magnetization right before each inversion pulse, and T_d is the delay time between the inversion and the first excitation pulse of a slice. After N excitation pulses and an interval between the next inversion pulse, the M_{ss} can be formulated as

$$M_{ss} = M_{eq}(1 - e^{-T_p/T_1}) + M(N-1)\cos\alpha \cdot e^{-T_p/T_1}, \quad [5]$$

where $T_p = TR - (N-1)\tau - T_d$. After substituting Eqs. [1] and [5] into Eq. [4] and dividing Eq. [4] by Eq. [2], the relation between $M(\infty)$ and $M(0)$ can be formulated as

$$\frac{M(0)}{M(\infty)} = (1 - 2e^{-T_d/T_1} + e^{-(T_p+T_d)/T_1}) \frac{(1 - e^{-\tau/T_1^*})}{(1 - e^{-\tau/T_1})} - \frac{M(N-1)}{M(\infty)} \cos\alpha \cdot e^{-(T_p+T_d)/T_1}, \quad [6]$$

where $\cos\alpha = e^{-\tau/T_1^*}/e^{-\tau/T_1}$. In the above equation, T_d , T_p , TR, and τ are known parameters, $M(\infty)/M(0)$ and T_1^* can be obtained by a three-parameter fitting of the measured signals, and $M(N-1)/M(\infty)$ can be calculated from Eq. [1] using the fitted parameters. Hence, T_1 can be solved from Eq. [6] without knowing the FA or needing τ and T_d to be short.

Pulse Sequences

To achieve whole-brain coverage of the rat brain in reasonable time, 2D multislice gradient-echo or 3D center-out

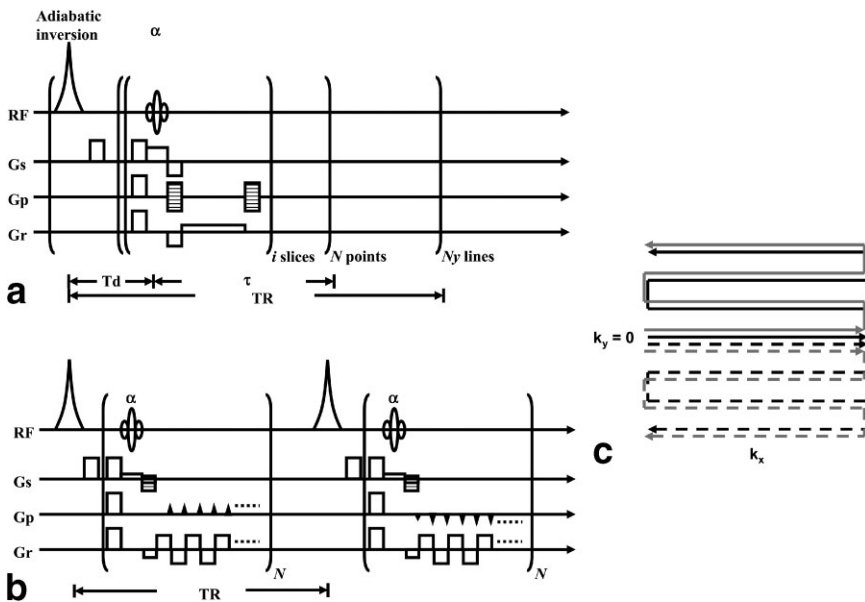


FIG. 1. Pulse sequence diagrams of the (a) 2D and (b) 3D Look-Locker T_1 mapping methods. In the 2D mode, i slices are acquired by gradient echo after a nonselective adiabatic inversion pulse. The same k -line of each slice is sampled N times along the recovery curve with a constant interval τ . In the 3D mode, center-out segmented gradient echo EPI is used to sample N time points along the signal recovery. (c) The trajectory of each segment of the 3D EPI sequence scans the upper or the lower half of the k -space. G_s : gradients in the slice-selection direction; G_p : gradients in the 2D phase-encoding direction; G_r : gradients in the readout direction; N_y : number of phase-encoding steps.

segmented EPI was used for data acquisition. Since inversion imperfection will lead to inaccurate T_1 estimation (41), a nonselective hyperbolic secant adiabatic pulse was used to provide B_1 -insensitive inversion. In the 2D mode (Fig. 1a), i slices are acquired by gradient-echo with T_d delay after the inversion pulse. The same line in the k -space of each slice is sampled N times along the recovery curve with a constant interval τ . Then the procedure is repeated for N_y times with different phase encoding gradients. To speed up the data acquisition, we evaluated using multiple excitations at each inversion time to acquire multiple k -space lines (42).

In the 3D mode, a center-out segmented gradient-echo EPI was used to acquire multiple lines of a plane in the k -space after each excitation (Fig. 1b). The trajectory of each segment starts from near the center of the k -space and traverses the upper or the lower half of the k -space (Fig. 1c). The acquisition is repeated N_{segment} times, each time with different phase shifts and gradient blip polarities to fill a plane in the k -space, and then repeated N_z times with different phase encoding gradients in the slice selection direction. The order of the phase encoding in the third dimension is also in a center-out fashion (i.e., $p_z = 0, \pm 1, \pm 2, \dots$). Using segmented EPI can shorten the image acquisition time while reducing the resolution blurring due to the T_2^* decay and off-resonance artifacts, such as geometric distortion, of single-shot EPI. With the center-out trajectory, high overall image SNR can be achieved due to the shorter TE.

Optimization on MnCl_2 Phantoms

Several compartments of MnCl_2 solutions with concentrations of 0, 1, 2, 5, 10, 20, 50, and 100 μM , respectively, were dissolved in double distilled water. The T_1 's of the MnCl_2 solutions were measured by a MFIR sequence and the 2D LL method. To find the optimal settings for accurate long T_1 measurement, the FA, interval τ , and number of sample N were changed from 5 to 30°, 50 to 500 ms, and 20

to 150, respectively. The setting giving good SNR and high accuracy in the low Mn^{2+} concentrations was used in the in vivo experiments. The 3D LL sequence was also tested and similar results were obtained (data not shown).

Animal Procedures

All animal work was done following the guidelines of the Animal Care and Use Committee and the Animal Health and Care Section of the National Institute of Neurological Disorders and Stroke, National Institutes of Health (Bethesda, MD, USA). Adult male Sprague-Dawley rats (body weights 155–330 g) were used in this study. Nine rats were scanned without Mn^{2+} injection and eight rats were scanned 34 h after stereotaxic MnCl_2 injection into the olfactory bulb (OB). For the stereotaxic injection, the animal was initially anesthetized by 5% isoflurane (in a 1:1:1 air:nitrogen:oxygen mixture), positioned in a stereotaxic frame, and maintained at 2–3% isoflurane during the surgery. A total of 50 nL aqueous solution of 100 mM MnCl_2 (Sigma-Aldrich Co., MO, USA) was slowly injected into either the left or the right side of the OB by a 0.5- μL Hamilton syringe (Reno, NV, USA) at Bregma 6.5 mm anterior, 2.0 mm lateral, and 2.5 mm dorsoventral according to the rat brain atlas (43). After the injection the needle was left in place for 5 min and then slowly retracted and removed. For MRI scans, rats were anesthetized by 5% isoflurane and placed in a custom-designed plastic stereotaxic holder. The anesthesia was maintained at 1–2% using a nose cone during the scanning. Rectal temperature was maintained at $37 \pm 1^\circ\text{C}$ by a heated water bath.

MRI

Images were acquired on an 11.7 T/31-cm horizontal magnet (Magnex Scientific Ltd., Abingdon, UK) interfaced to a Bruker Avance console (Bruker Medical GmbH, Germany) and equipped with a 9-cm gradient set that is capable of providing 60 G/cm strength and 80 μs rise time (Resonance Research,

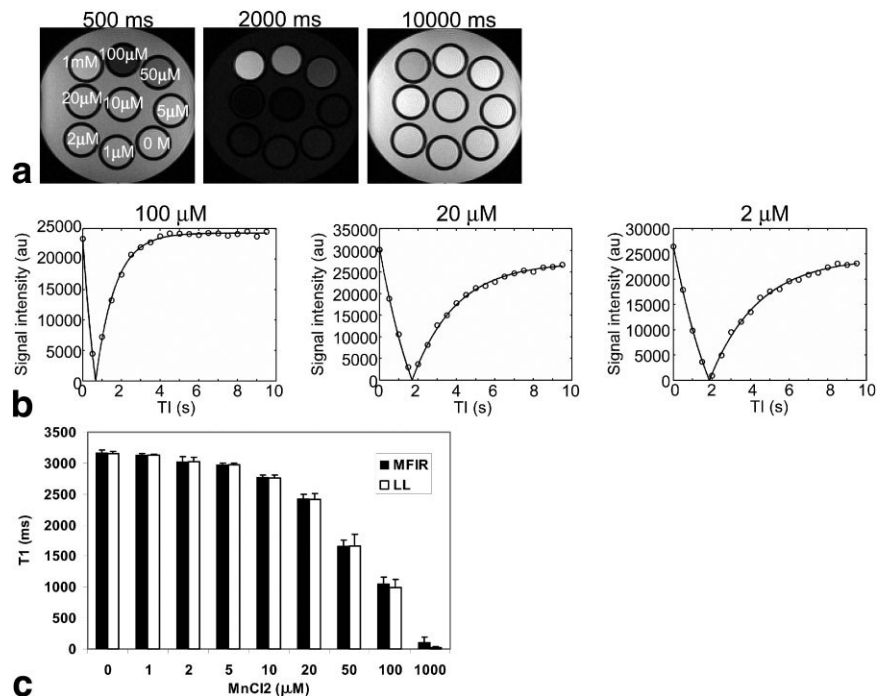


FIG. 2. (a) Images of the MnCl_2 -doped phantoms acquired at three different effective inversion times by the 2D Look-Locker (LL) sequence. (b) T_1 relaxation curves from three pixels with different MnCl_2 concentrations. The measured data (circles) matched very well with the nonlinear three-parameter fitting (solid lines). (c) The accuracy of the LL was compared with a modified fast inversion recovery spin-echo (MFIR) sequence in three independent measurements (error bar = STD). MnCl_2 concentrations as low as $2 \mu\text{M}$ (one-tailed t test, $P < 0.05$) can be differentiated from water by both T_1 mapping methods.

Billerica, MA, USA). In the phantom studies, data were acquired with a Bruker 35-mm transmit and receive volume coil. The T_1 's of different concentrations of MnCl_2 solutions were measured by a MFIR sequence using an optimal TR = 7.5 s, TE = 7 ms, field-of-view (FOV) = 2.56×2.56 cm, matrix = 128×128 , slice thickness = 1 mm, and inversion times of 8, 100, 200, 500, 1000, 1500, 2000, and 7450 ms.

For the tract-tracing studies, 3D T_1 W and 2D LL T_1 mapping images were obtained with a homemade, 35-mm diameter, transmit and receive, circular surface coil. The T_1 W images were acquired by a 3D rapid acquisition with relaxation enhancement (RARE) sequence with TR/TE = 300/10 ms and a RARE factor of 2. With FOV = $3.84 \times 2.56 \times 2.24$ cm and matrix size = $192 \times 128 \times 112$, 200 μm isotropic resolution can be obtained in 36 min. The 2D LL images were acquired with TR = 12 s, TE = 2.5 ms, $\alpha = 25^\circ$, $\tau = 500$ ms, $N = 20$. Forty-one coronal slices with FOV = 2.56×2.56 cm, matrix = 128×128 , thickness = 0.5 mm, and gap = 0.1 mm were used to cover the whole brain within 22 min.

Four control rats and three Mn^{2+} injected rats were scanned by the 3D LL sequence. 3D T_1 mapping was performed with a 90-mm volume transmit coil and a 30-mm saddle-shape surface receive coil. After adjusting high-order shimming, echo spacing, echo symmetry, and B_0 compensation, 3D LL data were acquired by center-out, segmented gradient-echo EPI with TR = 12 s, TE = 2.4 ms, $\alpha = 25^\circ$, $\tau = 500$ ms, and $N = 20$. To avoid resolution blurring due to the short T_2^* of the brain at 11.7 T, a bandwidth of 250 kHz and 16 echoes in one segment was used to keep the echo train length short. With a matrix size of $128 \times 128 \times 72$, 200- μm isotropic resolution can be obtained in 115 min.

Data Processing

The T_1 of each pixel was calculated in two steps using a custom-written program running in Matlab (The Math-

Works, Inc., Natick, MA, USA). First, the signal recovery of each pixel was fitted by the Levenburg-Marquardt nonlinear three-parameter curve-fitting algorithm. Then, the obtained parameters were substituted in Eq. [6] to solve the actual T_1 . The T_1 's of the MFIR images were calculated by the same nonlinear three-parameter curve fitting.

Region-of-interest (ROI) analysis was performed on 2D LL data using AMIDE (44). According to the rat brain atlas (43), many rectangular ROIs along the olfactory pathways were selected, including the OB, piriform cortex (Pir), anterior commissure (AC), accumbens nucleus (Acb), ventral pallidum (VP), lateral globus pallidus (LGP), medial forebrain (mfb), amygdala (Amy), and hippocampus (HC). Other regions, such as cortical gray matter (GM) in the somatosensory region and the muscle, were also inspected for comparison. One-tailed Student t test was used to compare the averaged T_1 in these regions between rats with and without Mn^{2+} injection.

RESULTS

MnCl_2 Phantoms

Figure 2a shows images of MnCl_2 phantoms acquired at effective TI of about 500, 2000, and 10000 ms, respectively, using the 2D LL sequence. The T_1 relaxation curves from pixels in the short, mid, and long T_1 compartments show good fit with the monoexponential function (Fig. 2b). The means and standard deviations (STDs) of the T_1 's from three independent measurements show good correspondence between the LL and MFIR methods (Fig. 2c). The mean absolute errors between the LL and MFIR are 0.95% ($T_1 = 3165$ ms), 0.60% ($T_1 = 3130$ ms), 0.51% ($T_1 = 3026$ ms), 1.09% ($T_1 = 2973$ ms), 1.62% ($T_1 = 2768$ ms), 2.32% ($T_1 = 2422$ ms), 4.19% ($T_1 = 1660$ ms), and 6.35% ($T_1 = 1050$ ms). The errors are less than 6.5% for $T_1 > 1000$ ms and are less than 2.5% for $T_1 > 2500$ ms, indicating better accuracy for the long T_1 compartments. Both

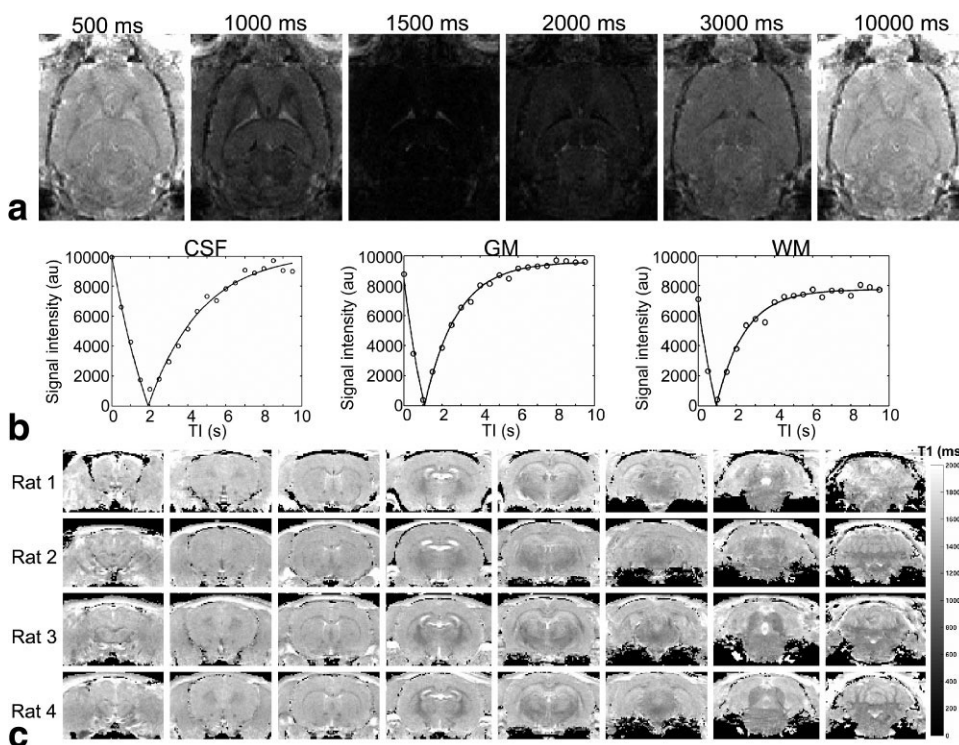


FIG. 3. (a) Axial images of a normal rat without MnCl_2 injection acquired at various effective inversion times using the 3D Look-Locker sequence. The segmented EPI shows high SNR without significant artifacts or distortion in the brain, except regions close to the nasal cavity and ear canals. (b) Measured T_1 relaxation curves (circles) and the fitting (solid lines) from three pixels in the CSF, gray matter (GM), and white matter (WM), respectively. The CSF data didn't match the monoexponential model well near the zero-crossing point. (c) Coronal sections of the T_1 maps from four rats show good contrast between the cortex and white matter structures.

T_1 mapping methods can differentiate Mn^{2+} concentrations as low as $2 \mu\text{M}$ from water without Mn^{2+} ($P < 0.05$; one-tailed t test). By a linear fitting of the relaxation rates ($R_1 = 1/T_1$) at different concentrations, the relaxivity of aqueous MnCl_2 was measured to be $6.3 \text{ s}^{-1} \text{ mM}^{-1}$ by the MFIR, but was slightly higher ($6.9 \text{ s}^{-1} \text{ mM}^{-1}$) by the LL due to a higher error for the short T_1 compartments.

T_1 Maps of Rat Brain

Figure 3 is an example of the 3D LL T_1 mapping of a rat brain without Mn^{2+} injection. With center-out segmented EPI, the 3D T_1 maps show good SNR without much susceptibility artifacts, geometric distortion, or resolution blurring. Images of an axial section obtained at different effective TIs show good SNR and low artifacts or distortion in the brain, except in parts of the olfactory bulb, which is close to the nasal cavity (Fig. 3a). The T_1 relaxation curves of pixels selected from the cerebrospinal fluid (CSF), gray matter, and white matter (WM) present distinct signal recovery trends and fit well with the monoexponential curves except in CSF (Fig. 3b). Figure 3c shows coronal sections of the calculated T_1 maps from four rats. Clear contrasts among the CSF, cortex, thalamus, and WM structures, such as corpus callosum, can be observed. The average T_1 of five rats measured by the 2D LL is about 1650 ms in the GM, 1370 ms in the WM, and 2430 ms in the CSF (Table 1).

Figure 4 shows slices from the 3D T_1 map of a rat brain at 34 h after Mn^{2+} injected in the OB. Mn^{2+} -induced T_1 decreases can be observed in the ipsilateral side of the brain from OB, anterior olfactory nucleus, Pir, olfactory tubercle, orbital cortex, and putamen to Amy, as well as other structures like internal capsule and lateral hypothalamus (Fig. 4). The neuronal tracts to the contralateral Pir

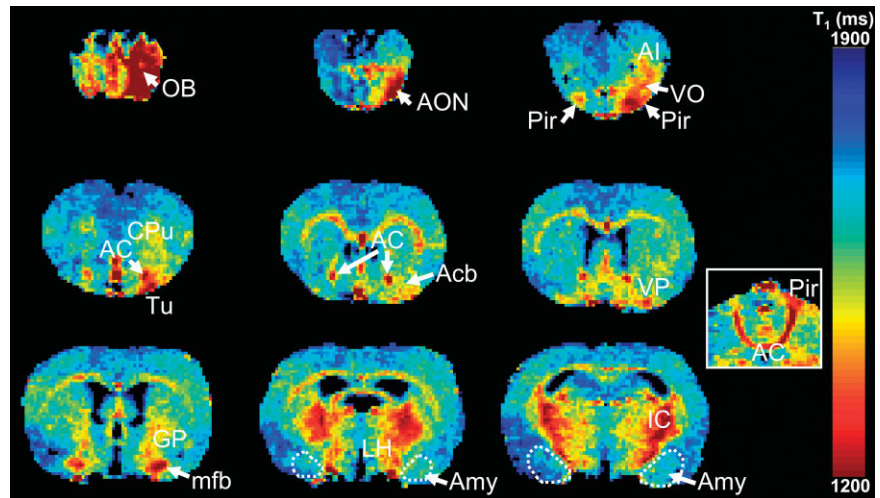
through the AC are also clearly delineated (the inlet in Fig. 4). Comparing the T_1 's in ROIs between rats with and without Mn^{2+} injection, significant T_1 reductions can be found in OB, Pir, AC, Acb, VP, LGP, mfb, and Amy, but not in GM, HC, or muscle (Fig. 5). Large T_1 changes can be seen in the OB (about 620 ms; 36% T_1 change) and Pir (about 300 ms; 21% T_1 change). They were also the only regions that were detected by the T_1 W images used in this study. The smallest T_1 change detected in the selected ROIs is about 100 ms in LGP (7% T_1 change). Using the relaxivity of aqueous MnCl_2 to estimate the tissue concentrations of Mn^{2+} , the structures with concentrations from high to low are OB ($47.9 \mu\text{M}$), Pir ($25.8 \mu\text{M}$), VP ($13.2 \mu\text{M}$), AC ($12.3 \mu\text{M}$), Acb ($11.2 \mu\text{M}$), mfb ($10.9 \mu\text{M}$), LGP ($7.6 \mu\text{M}$), and Amy ($6.8 \mu\text{M}$).

TABLE 1
Rat Brain T_1 's measured at 11.7 T

Brain regions	T_1 (ms)
Cerebrospinal fluid	2430 ± 172.3
Cortex	
Olfactory bulb	1713 ± 138.8
Primary somatosensory cortex	1597 ± 52.65
Hippocampus	1611 ± 102.6
Amygdala	1656 ± 98.68
White matter	
Corpus callosum	1346 ± 40.79
Anterior commissure	1393 ± 117.5

Note. Means and standard deviations of the T_1 's were from five rats using the 2D Look-Locker sequence.

FIG. 4. Coronal sections from the 3D T_1 map of a rat 34 h after Mn^{2+} was injected in the OB. Cortical and subcortical areas as well as tracts in the olfactory pathways to the ipsilateral amygdala (please note the asymmetric enhancement in the circled area by dashed lines) and the contralateral Pir can be identified. The inlet on the right is a horizontal section showing the connection from ipsilateral to contralateral Pir through AC. AC, anterior commissure; Acb, accumbens nucleus; AI, anterior insular; Amy, amygdala; AON, anterior olfactory nucleus; CPu, caudate putamen; IC, internal capsule; GP, globus pallidus; LH, lateral hypothalamic area; mfb, medial forebrain; Pir, piriform cortex; Tu, olfactory tubercle; VO, ventral orbital cortex; VP, ventral pallidum.



DISCUSSION

Due to the wide dynamic range of the T_1 reduction in MEMRI, T_1W imaging cannot provide enough sensitivity for detecting the full range of concentrations of the contrast agent. The LL T_1 mapping technique provides similar sensitivity to the full T_1 range with whole-brain coverage in reasonable time. T_1 maps showed high contrast in various anatomic structures. In the olfactory tract tracing experiments with Mn^{2+} injected into the OB, T_1 maps clearly identified tracks along the olfactory pathway to the amygdala in individual animals. Although we didn't find T_1 change in other regions that are known to be connected to the olfactory pathway, such as the hippocampus, this may be due to low Mn^{2+} concentration or partial volume effects of these small structures at the resolution used. It may be possible to see these pathways by injecting a higher dose of Mn^{2+} as has been done for many MEMRI neuronal tract-tracing studies (16,22,23,34).

Neurotoxicity caused by manganese can be an issue when using it as a contrast agent in human or animal studies. In this work, we used a low dose of manganese (about 0.5 mg/kg of the brain weight), which is less than the daily dietary dose of 10 mg/kg body wt (45). With such

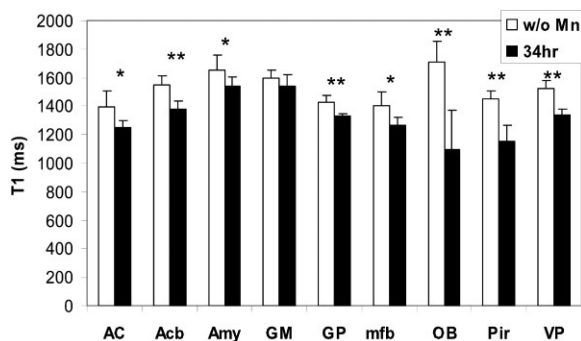


FIG. 5. Compared to rats without manganese injection ($N = 5$), significant decrease in T_1 's can be observed at various locations in the olfactory pathways 34 h after manganese injection in the olfactory bulb ($N = 6$). T_1 change as small as 100 ms can be observed (in GP).

a low injection dosage, it was still possible to detect significant changes in regions of the brain such as the amygdala that previously were only detected through group averaging (34). Therefore, with the enhanced sensitivity of the T_1 mapping procedure, the dosage of manganese can be reduced.

T_1 mapping provides the potential to quantify Mn^{2+} concentrations in tissues. Indeed, in the phantom as little as 2 μM $MnCl_2$ could be detected. Since Mn^{2+} quantitation has not yet been performed in tissue extracts, the relaxivity for deriving the tissue Mn^{2+} concentration from T_1 is not known. Assuming the relaxivity of Mn^{2+} in tissues is the same as in water, the lowest concentration observed in the ROIs we chose was in the amygdala, which contained less than 7 μM Mn^{2+} . Because the relaxivity in tissue is expected to be higher than that in water (46), the actual Mn^{2+} concentration should be significantly lower. In addition, the concentration could provide information on the rate of Mn^{2+} progression along the pathway. The Mn^{2+} concentrations in different regions can be due to the difference in regional release/uptake rates, cell density, size of neuronal fiber, crossing of synapses, etc. It will become of growing importance to quantitate effects of Mn^{2+} to separate these different effects. Assuming the same relaxivity for all tissues, the concentrations of manganese can be divided into four groups (from highest to lowest): (1) OB; (2) Pir; (3) VP, AC, Acb, mfb; (4) LGP and Amy. This matches their distances from the OB.

The rat brain T_1 measured in cortical structures were in the range of 1.6 to 1.7 s. Compared to other rat brain T_1 's reported at high fields, these values are somewhat shorter. For example, cortical T_1 has been reported as 1.76 s at 8.5 T (47) and 1.81 or 1.99 s at 9.4 T (13,48). One paper reported mouse cortical T_1 at 11.7 T to be 1.9 s (49). The difference may be due to the accuracy of the different T_1 measurement techniques used, partial volume effects (resolution and ROI size), or animal species and details of diet. It may also be that the LL sequence used caused some magnetization transfer contrast effects that would cause a shortening of T_1 (50). The relatively poor fit of the CSF T_1 relaxation curve (Fig. 3b) indicates that there were probably partial volume effects on T_1 at the resolution used. The

motion of the CSF flow could also make the measured T_1 shorter and the signal deviated from the ideal relaxation curve.

The LL technique used relied on gradient-echoes to acquire the signal. Hence, it is sensitive to susceptibility artifacts caused by air-tissue interfaces, especially at the high field of 11.7 T used in these studies. In the 2D T_1 maps, important regions in the rat olfactory pathway such as the ventral part of the hippocampus and the entorhinal cortex were affected by the signal drop-out due to the nearby ear canals. The 3D T_1 maps showed fewer susceptibility artifacts in these regions due to the use of higher bandwidth and 3D acquisition. However, geometric distortion was observed in the OB due to poorer shimming near the nasal cavity.

The parameters for the LL T_1 mapping used in this study were optimized for measuring low concentrations of the contrast agent through the use of a long τ and a FA > 20°. We also incorporated an algorithm suitable for quantitative long T_1 's and for multislice acquisition. From the phantom tests, high accuracy was achieved, especially for the long T_1 compartments. Although the error in the short T_1 range was higher due to fewer samples being acquired in the fast rising period of the inversion recovery, this was not a serious problem because regions with large T_1 changes are easy to detect and the focus of the optimization was on the low concentration range for Mn^{2+} . This is different from other studies that developed the LL techniques for clinical use, where they utilized a much shorter τ to get high accuracy for $T_1 < 1000$ ms (39,51,52). Although the parameters were experimentally optimized in this study, they may not be the optimal. Since SNR and accuracy of LL T_1 measurement have a complex relationship with TR, τ , α , and N , further optimization can be conducted by numerical methods (41).

In this study, 2D T_1 mapping data can be acquired in about 20 min and the 3D data took nearly 2 h to obtain 200- μm isotropic resolution. Although it is acceptable in some animal studies, it makes mapping with higher resolution, e.g., 100 μm isotropic, or performing dynamic studies difficult. Since the T_2^* limits the echo train length of each segment, reducing the data acquisition time by acquiring more echoes in one segment will require increasing the sampling bandwidth at the expense of reduced SNR. One way to further shorten the data acquisition time is to use multiple shots at each TI (42,53). Since shot-to-shot T_1 relaxation will produce additional weighting to different k -space lines, banding artifacts will occur in the image even with center-out phase encoding and will limit the useable number of shots. Another way to cut down the acquisition time is to use a shorter TR. This can be accomplished with a saturation pulse before the inversion pulse to eliminate the need for full relaxation (40). However, to get good accuracy for long T_1 compartments, the saturation time and τ cannot be made too short; thus, the actual shortening in TR will not be that large. Finally, recent advances in parallel imaging techniques may provide a feasible solution to reduce the acquisition time (54,55). Preliminary results with four element arrays for the rodent brain indicate that two- to three-fold speedup can be achieved. The loss in SNR associated with speedup using parallel imaging will be offset to some extent by gains in

sensitivity using the smaller coils required by parallel imaging arrays (56).

Some studies have used T_1W imaging with 100- μm resolution in times comparable to that used for the T_1 mapping reported in this study at 200 μm . The specific advantages and disadvantages of higher-resolution T_1W imaging and more quantitative but lower resolution T_1 mapping depends on the SNR, the CNR, and the size of the structure of interest. Since increasing the resolution will generally reduce the SNR, the CNR of small structures will not necessarily be increased by the reduced partial volume effect. If CNR is not high enough, T_1 mapping will have a better chance to detect the manganese enhancement. But if the size of the structure of interest is smaller than a voxel in the lower-resolution T_1 mapping then it may be advantageous to use T_1W imaging. However, with implementation of parallel imaging strategies for rodents it should be possible to obtain quantitative T_1 maps at 100- μm resolution or lower in a similar amount of time and in this way have the quantitative advantage of T_1 maps with very high resolution.

CONCLUSION

Using the Look-Locker technique, whole-brain 3D T_1 mapping with 200- μm isotropic resolution can be obtained in less than 2 h. With optimized parameters and an algorithm for long T_1 measurement, Mn^{2+} concentrations as low as 2 μM can be detected in vitro and T_1 changes as small as 7% can be detected in vivo. MEMRI neuronal tract tracing to regions far from the Mn^{2+} injection site, such as the amygdala, can be observed in the olfactory pathways of individual rats.

ACKNOWLEDGMENTS

We thank Dr. Hellmut Merkle for building the coils; Dr. Shella Keilholz for helping with the sequence; and Dr. Galit Pelled and Ms. Torri Wilson for guidance in animal preparations.

REFERENCES

1. Koretsky AP, Silva AC. Manganese-enhanced magnetic resonance imaging (MEMRI). *NMR Biomed* 2004;17:527-531.
2. Silva AC, Lee JH, Aoki I, Koretsky AP. Manganese-enhanced magnetic resonance imaging (MEMRI): methodological and practical considerations. *NMR Biomed* 2004;17:532-543.
3. Watanabe T, Frahm J, Michaelis T. Functional mapping of neural pathways in rodent brain in vivo using manganese-enhanced three-dimensional magnetic resonance imaging. *NMR Biomed* 2004;17:554-568.
4. Aoki I, Naruse S, Tanaka C. Manganese-enhanced magnetic resonance imaging (MEMRI) of brain activity and applications to early detection of brain ischemia. *NMR Biomed* 2004;17:569-580.
5. Van der Linden A, Van Meir V, Tindemans I, Verhoye M, Balthazart J. Applications of manganese-enhanced magnetic resonance imaging (MEMRI) to image brain plasticity in song birds. *NMR Biomed* 2004;17:602-612.
6. Wadghiri YZ, Blind JA, Duan X, Moreno C, Yu X, Joyner AL, Turnbull DH. Manganese-enhanced magnetic resonance imaging (MEMRI) of mouse brain development. *NMR Biomed* 2004;17:613-619.
7. Pautler RG. In vivo, trans-synaptic tract-tracing utilizing manganese-enhanced magnetic resonance imaging (MEMRI). *NMR Biomed* 2004;17:595-601.

8. Drapeau P, Nachshen DA. Manganese fluxes and manganese-dependent neurotransmitter release in presynaptic nerve endings isolated from rat brain. *J Physiol* 1984;348:493–510.
9. Sloot WN, Gramsbergen JB. Axonal transport of manganese and its relevance to selective neurotoxicity in the rat basal ganglia. *Brain Res* 1994;657:124–132.
10. London RE, Toney G, Gabel SA, Funk A. Magnetic resonance imaging studies of the brains of anesthetized rats treated with manganese chloride. *Brain Res Bull* 1989;23:229–235.
11. Newland MC, Ceckler TL, Kordower JH, Weiss B. Visualizing manganese in the primate basal ganglia with magnetic resonance imaging. *Exp Neurol* 1989;106:251–258.
12. Lin YJ, Koretsky AP. Manganese ion enhances T_1 -weighted MRI during brain activation: an approach to direct imaging of brain function. *Magn Reson Med* 1997;38:378–388.
13. Duong TQ, Silva AC, Lee SP, Kim SG. Functional MRI of calcium-dependent synaptic activity: cross correlation with CBF and BOLD measurements. *Magn Reson Med* 2000;43:383–392.
14. Aoki I, Tanaka C, Takegami T, Ebisu T, Umeda M, Fukunaga M, Fukuda K, Silva AC, Koretsky AP, Naruse S. Dynamic activity-induced manganese-dependent contrast magnetic resonance imaging (DAIM MRI). *Magn Reson Med* 2002;48:927–933.
15. Morita H, Ogino T, Seo Y, Fujiki N, Tanaka K, Takamata A, Nakamura S, Murakami M. Detection of hypothalamic activation by manganese ion contrasted T_1 -weighted magnetic resonance imaging in rats. *Neurosci Lett* 2002;326:101–104.
16. Pautler RG, Silva AC, Koretsky AP. In vivo neuronal tract tracing using manganese-enhanced magnetic resonance imaging. *Magn Reson Med* 1998;40:740–748.
17. Watanabe T, Michaelis T, Frahm J. Mapping of retinal projections in the living rat using high-resolution 3D gradient-echo MRI with Mn^{2+} -induced contrast. *Magn Reson Med* 2001;46:424–429.
18. Lin CP, Tseng WY, Cheng HC, Chen JH. Validation of diffusion tensor magnetic resonance axonal fiber imaging with registered manganese-enhanced optic tracts. *Neuroimage* 2001;14:1035–1047.
19. Saleem KS, Pauls JM, Augath M, Trinath T, Prause BA, Hashikawa T, Logothetis NK. Magnetic resonance imaging of neuronal connections in the macaque monkey. *Neuron* 2002;34:685–700.
20. Van der Linden A, Verhoye M, Van Meir V, Tindemans I, Eens M, Absil P, Balhazart J. In vivo manganese-enhanced magnetic resonance imaging reveals connections and functional properties of the songbird vocal control system. *Neuroscience* 2002;112:467–474.
21. Pautler RG, Mongeau R, Jacobs RE. In vivo trans-synaptic tract tracing from the murine striatum and amygdala utilizing manganese enhanced MRI (MEMRI). *Magn Reson Med* 2003;50:33–39.
22. Leergaard TB, Bjaalie JG, Devor A, Wald LL, Dale AM. In vivo tracing of major rat brain pathways using manganese-enhanced magnetic resonance imaging and three-dimensional digital atlas. *Neuroimage* 2003;20:1591–1600.
23. Allegrini PR, Wiessner C. Three-dimensional MRI of cerebral projections in rat brain in vivo after intracortical injection of $MnCl_2$. *NMR Biomed* 2003;16:252–256.
24. Aoki I, Wu YJ, Silva AC, Lynch RM, Koretsky AP. In vivo detection of neuroarchitecture in the rodent brain using manganese-enhanced MRI. *Neuroimage* 2004;22:1046–1059.
25. Watanabe T, Natt O, Boretius S, Frahm J, Michaelis T. In Vivo 3D MRI staining of mouse brain after subcutaneous application of $MnCl_2$. *Magn Reson Med* 2002;48:852–859.
26. Barbeau A. Manganese and extrapyramidal disorders (a critical review and tribute to Dr. George C. Cotzias). *Neurotoxicology* 1984;5:13–35.
27. Ahrens ET, Rothbacher U, Jacobs RE, Fraser SE. A model for MRI contrast enhancement using T_1 agents. *Proc Natl Acad Sci USA* 1998;95:8443–8448.
28. Mugler JP, 3rd, Brookeman JR. Three-dimensional magnetization-prepared rapid gradient-echo imaging (3D MP RAGE). *Magn Reson Med* 1990;15:152–157.
29. Lee JH, Garwood M, Menon R, Adriany G, Andersen P, Truwit CL, Ugurbil K. High contrast and fast three-dimensional magnetic resonance imaging at high fields. *Magn Reson Med* 1995;34:308–312.
30. Ikonomidou VN, van Gelderen P, de Zwart JA, Fukunaga M, Duyn JH. Optimizing brain tissue contrast with EPI: A simulated annealing approach. *Magn Reson Med* 2005;54:373–385.
31. Deichmann R, Good CD, Josephs O, Ashburner J, Turner R. Optimization of 3-D MP-RAGE sequences for structural brain imaging. *Neuroimage* 2000;12:112–127.
32. Deichmann R, Schwarzbauer C, Turner R. Optimisation of the 3D MDEFT sequence for anatomical brain imaging: technical implications at 1.5 and 3 T. *Neuroimage* 2004;21:757–767.
33. Lee JH, Silva AC, Merkle H, Koretsky AP. Manganese-enhanced magnetic resonance imaging of mouse brain after systemic administration of $MnCl_2$: dose-dependent and temporal evolution of T_1 contrast. *Magn Reson Med* 2005;53:640–648.
34. Cross DJ, Minoshima S, Anzai Y, Flexman JA, Keogh BP, Kim Y, Maravilla KR. Statistical mapping of functional olfactory connections of the rat brain in vivo. *Neuroimage* 2004;23:1326–1335.
35. Ogg RJ, Kingsley PB. Optimized precision of inversion-recovery T_1 measurements for constrained scan time. *Magn Reson Med* 2004;51:625–630.
36. Deoni SC, Rutt BK, Peters TM. Rapid combined T_1 and T_2 mapping using gradient recalled acquisition in the steady state. *Magn Reson Med* 2003;49:515–526.
37. Look DC, Locker DR. Time saving in measurement of NMR and EPR relaxation times. *Rev Sci Instrum* 1970;41:250–251.
38. Crawley AP, Henkelman RM. A comparison of one-shot and recovery methods in T_1 imaging. *Magn Reson Med* 1988;7:23–34.
39. Brix G, Schad LR, Deimling M, Lorenz WJ. Fast and precise T_1 imaging using a TOMROP sequence. *Magn Reson Imaging* 1990;8:351–356.
40. Steinhoff S, Zaitsev M, Zilles K, Shah NJ. Fast T_1 mapping with volume coverage. *Magn Reson Med* 2001;46:131–140.
41. Zaitsev M, Steinhoff S, Shah NJ. Error reduction and parameter optimization of the TAPIR method for fast T_1 mapping. *Magn Reson Med* 2003;49:1121–1132.
42. Lee JH. PURR-TURBO: a novel pulse sequence for longitudinal relaxographic imaging. *Magn Reson Med* 2000;43:773–777.
43. Paxinos G, Watson C. The rat brain in stereotaxic coordinates. San Diego: Academic Press; 1998.
44. Loening A, Gambhir S. AMIDE: a free software tool for multimodality medical image analysis. *Mol Imaging* 2003;2:131–137.
45. Subcommittee on Laboratory Animal Nutrition CoAN, Board on Agriculture, National Research Council. Nutrient Requirements of Laboratory Animals: National Academy Press; 1995.
46. Kang YS, Gore JC. Studies of tissue NMR relaxation enhancement by manganese. Dose and time dependences. *Invest Radiol* 1984;19:399–407.
47. Calamante F, Lythgoe MF, Pell GS, Thomas DL, King MD, Busza AL, Sotak CH, Williams SR, Ordidge RJ, Gadian DG. Early changes in water diffusion, perfusion, T_1 , and T_2 during focal cerebral ischemia in the rat studied at 8.5 T. *Magn Reson Med* 1999;41:479–485.
48. Schwarcz A, Berente Z, Osz E, Doczi T. Fast in vivo water quantification in rat brain oedema based on T_1 measurement at high magnetic field. *Acta Neurochir (Wien)* 2002;144:811–815; discussion 815–816.
49. Ahrens ET, Dubowitz DJ. Peripheral somatosensory fMRI in mouse at 11.7 T. *NMR Biomed* 2001;14:318–324.
50. Wolff SD, Balaban RS. Magnetization transfer contrast (MTC) and tissue water proton relaxation in vivo. *Magn Reson Med* 1989;10:135–144.
51. Kay I, Henkelman RM. Practical implementation and optimization of one-shot T_1 imaging. *Magn Reson Med* 1991;22:414–424.
52. Gowland PA, Leach MO. Fast and accurate measurements of T_1 using a multi-readout single inversion-recovery sequence. *Magn Reson Med* 1992;26:79–88.
53. Henderson E, McKinnon G, Lee TY, Rutt BK. A fast 3D look-locker method for volumetric T_1 mapping. *Magn Reson Imaging* 1999;17:1163–1171.
54. Pruessmann KP, Weiger M, Scheidegger MB, Boesiger P. SENSE: sensitivity encoding for fast MRI. *Magn Reson Med* 1999;42:952–962.
55. Sodickson DK, Manning WJ. Simultaneous acquisition of spatial harmonics (SMASH): fast imaging with radiofrequency coil arrays. *Magn Reson Med* 1997;38:591–603.
56. de Zwart JA, Ledden PJ, van Gelderen P, Bodurka J, Chu R, Duyn JH. Signal-to-noise ratio and parallel imaging performance of a 16-channel receive-only brain coil array at 3.0 Tesla. *Magn Reson Med* 2004;51:22–26.